Astronomy & Astrophysics manuscript no. article_fin
February 14, 2013

Coronagraphic phase diversity: performance study and laboratory demonstration

B. Paul[1 2 3], J.-F. Sauvage[1 3], and L. M. Mugnier[1 3]

[1] Onera - The French Aerospace Lab, F-92322 Chatillon France
[2] Aix Marseille Université, CNRS, LAM (Laboratoire d'Astrophysique de Marseille) UMR 7326, 13388, Marseille, France
[3] Groupement d'intérêt scientifique PHASE (Partenariat Haute résolution Angulaire Sol et Espace) between Onera, Observatoire de Paris, CNRS, Université Diderot, Laboratoire d'Astrophysique de Marseille and Institut de Planétologie et d'Astrophysique de Grenoble

Received <date>; accepted <date>

ABSTRACT

Context. The final performance of current and future instruments dedicated to exoplanet detection and characterization (such as SPHERE on the European Very Large Telescope, GPI on Gemini North, or future instruments on Extremely Large Telescopes) is limited by uncorrected quasi-static aberrations. These aberrations create long-lived speckles in the scientific image plane, which can easily be mistaken for planets.
Aims. Common adaptive optics systems require dedicated components to perform wave-front analysis. The ultimate wave-front measurement performance is thus limited by the unavoidable differential aberrations between the wavefront sensor and the scientific camera. To reach the level of detectivity required by high-contrast imaging, these differential aberrations must be estimated and compensated for. In this paper, we characterize and experimentally validate a wave-front sensing method that relies on focal-plane data.
Methods. Our method, called COFFEE (for COronagraphic Focal-plane wave-Front Estimation for Exoplanet detection), is based on a Bayesian approach, and it consists in an extension of phase diversity to high-contrast imaging. It estimates the differential aberrations using only two focal-plane coronagraphic images recorded from the scientific camera itself.
Results. We first present a thorough characterization of COFFEE's performance by means of numerical simulations. This characterization is then compared with an experimental validation of COFFEE using an in-house adaptive optics bench and an apodized Roddier & Roddier phase mask coronagraph. An excellent match between experimental results and the theoretical study is found. Lastly, we present a preliminary validation of COFFEE's ability to compensate for the aberrations upstream of a coronagraph.

Key words. instrumentation: adaptive optics, instrumentation: high angular resolution, techniques: image processing, methods: numerical, methods: laboratory, telescopes

1. Introduction

Exoplanet imaging is one of the main challenges in today's astronomy. A direct observation of these planets can provide information on both the chemical composition of their atmospheres and their temperatures. Such observations have recently been made possible (Kalas et al. (2008), Marois et al. (2008), Lagrange et al. (2009)), but only thanks to their high mass or their wide apparent distance from their host star.
Being able to image an object as faint as an extra-solar planet very close to its parent star requires the use of extreme AO (XAO) systems coupled to a high-contrast imaging technique, such as coronagraphy. Instruments dedicated to exoplanet imaging using these two techniques (SPHERE on the VLT, Beuzit et al. (2007), GPI on Gemini North, Macintosh et al. (2008)) are currently being integrated. The performance of such systems is limited by residual speckles on the detector. These speckles, which originate in quasi-static non common path aberrations (NCPA), strongly decrease the extinction provided by the coronagraph and can be difficult to distinguish from an exoplanet. To achieve the ultimate system performance, these aberrations must be measured and compensated for. The current-generation instruments, SPHERE and GPI, respectively rely on phase diversity (Gonsalvez (1982)) and an interferometry approach (Wallace et al. (2010)) to compensate for these NCPA.
Several techniques dedicated to high-contrast imaging system optimization have been proposed for future systems. Some of them rely on a dedicated wave-front sensing hardware (Guyon et al. (2009)), others use scientific focal plane data assuming small aberrations. Speckle nulling iterative techniques (Bordé & Traub (2006), Give'on et al. (2007)) estimate the electric field in the detector plane using at least three images. The technique proposed by Baudoz et al. (2006) relies on a modification of the imaging system, but requires only one image. These techniques aim at minimizing the energy in a chosen area ("Dark Hole"), leading to a contrast optimization on the detector (Trauger et al. (2010), Baudoz et al. (2012)) in a closed loop process.
We have recently proposed a focal-plane wave-front sensor, COFFEE (Sauvage et al. (2012)), which is an extension of conventional phase diversity (Mugnier et al. (2006)) to a coronagraphic system. Since COFFEE uses focal-plane images, it is possible to characterize the whole bench without any differential aberration. This method requires only two focal-plane images to estimate the aberrations upstream of the coronagraph without any modification of the coronagraphic imaging system or assuming small aberrations. COFFEE's principle and its application to the apodized Roddier & Roddier phase mask (ARPM)

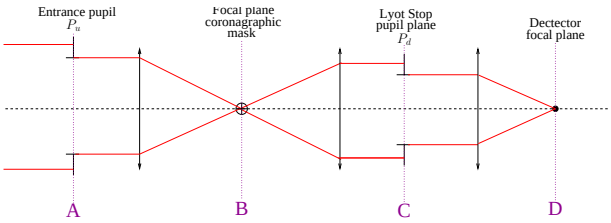

Fig. 1. Coronagraphic imaging instrument: principle

are described in Section 2. In Section 3, we evaluate the quality of NCPA estimation by realistic simulations. In Section 4, we present the experimental results from the laboratory demonstration of COFFEE on an in-house adaptive optics bench (BOA) with an ARPM. Section 5 concludes the paper.

2. COFFEE: principle

2.1. Extension of phase diversity to coronagraphic images

Figure 1 describes the coronagraphic imaging scheme considered in this paper. We consider four successive planes denoted A (circular entrance pupil of diameter D_u), B (coronagraphic focal plane), C (Lyot Stop), and D (detector plane). The optical aberrations are considered as static and introduced in the pupil planes A and C. The coronagraphic device is composed of a focal plane mask located in plane B and a Lyot Stop situated in plane C. No particular assumption is made on the pupil shape or intensity. Thus, the description of COFFEE is compatible with several coronagraphic devices. COFFEE uses two images, $\boldsymbol{i}_c^{\mathrm{f}}$ and $\boldsymbol{i}_c^{\mathrm{d}}$, recorded on the detector (plane D in Figure 1) that, as in phase diversity, differ from a known aberration, $\boldsymbol{\phi}_{div}$, to estimate aberrations both upstream ($\boldsymbol{\phi}_u$) and downstream ($\boldsymbol{\phi}_d$) of the coronagraph.

Considering the calibration of the instrument with an unresolved object, we use the following imaging model:

$$\begin{aligned}\boldsymbol{i}_c^{\mathrm{foc}} &= \alpha.\boldsymbol{h}_{\mathrm{det}} \star \boldsymbol{h}_c(\boldsymbol{\phi}_u, \boldsymbol{\phi}_d) + \boldsymbol{n}^{\mathrm{foc}} + \beta \\ \boldsymbol{i}_c^{\mathrm{div}} &= \alpha.\boldsymbol{h}_{\mathrm{det}} \star \boldsymbol{h}_c(\boldsymbol{\phi}_u + \boldsymbol{\phi}_{div}, \boldsymbol{\phi}_d) + \boldsymbol{n}^{\mathrm{div}} + \beta\end{aligned} \tag{1}$$

where α is the incoming flux, $\boldsymbol{h}_c$ the coronagraphic "point spread function" (PSF) of the instrument (i.e. the response of a coronagraphic imaging system to a point source), $\boldsymbol{h}_{\mathrm{det}}$ the known detector PSF, $\boldsymbol{n}^{\mathrm{foc}}$ and $\boldsymbol{n}^{\mathrm{div}}$ are the measurement noises, β is a uniform background (offset), and $\star$ denotes the discrete convolution operation. Such an imaging model can be used for any coronagraphic PSF expression $\boldsymbol{h}_c$. The measurement noises $\boldsymbol{n}^{\mathrm{foc}}$ and $\boldsymbol{n}^{\mathrm{div}}$ comprise both photon and detector noises. Because calibration is assumed to be performed with high flux levels, we adopt a non-stationary white Gaussian model, which is a good approximation of a mix of photon and detector noises. Its variance is the sum of the photon and detector noise variances: $\boldsymbol{\sigma}_n^2[t] = \boldsymbol{\sigma}_{\mathrm{ph}}^2[t] + \sigma_{\mathrm{det}}^2$ (Mugnier et al. (2004)), with t the pixel position in the detector plane. The former can be estimated as the image itself thresholded to positive values, and the latter can be calibrated prior to the observations.

We adopt a maximum *a posteriori* (MAP) approach and estimate the aberrations ϕ_u and ϕ_d, the flux α, and the background β that minimize the neg-log-likelihood of the data, potentially penalized by regularization terms on $\boldsymbol{\phi}_u$ and $\boldsymbol{\phi}_d$ designed to enforce smoothness of the sought phases:

$$(\hat{\alpha}, \hat{\beta}, \hat{\boldsymbol{\phi}_u}, \hat{\boldsymbol{\phi}_d}) = \underset{\alpha,\beta,\boldsymbol{\phi}_u,\boldsymbol{\phi}_d}{\arg\min}\, J(\alpha, \beta, \boldsymbol{\phi}_u, \boldsymbol{\phi}_d) \tag{2}$$

where

$$\begin{aligned}J(\alpha, \beta, \boldsymbol{\phi}_u, \boldsymbol{\phi}_d) = \frac{1}{2}\left\| \frac{\boldsymbol{i}_c^{\mathrm{foc}} - (\alpha.\boldsymbol{h}_{\mathrm{d}} \star \boldsymbol{h}_c(\boldsymbol{\phi}_u, \boldsymbol{\phi}_d) + \beta)}{\boldsymbol{\sigma}_n^{\mathrm{foc}}} \right\|^2 \\ + \frac{1}{2}\left\| \frac{\boldsymbol{i}_c^{\mathrm{div}} - (\alpha.\boldsymbol{h}_{\mathrm{d}} \star \boldsymbol{h}_c(\boldsymbol{\phi}_u + \boldsymbol{\phi}_{div}, \boldsymbol{\phi}_d) + \beta)}{\boldsymbol{\sigma}_n^{\mathrm{div}}} \right\|^2 \\ + \mathcal{R}(\boldsymbol{\phi}_u) + \mathcal{R}(\boldsymbol{\phi}_d)\end{aligned} \tag{3}$$

where $\|\boldsymbol{x}\|^2$ denotes the sum of squared pixel values of map $\boldsymbol{x}$, $\boldsymbol{\sigma}_n^{\mathrm{foc}}$, and $\boldsymbol{\sigma}_n^{\mathrm{div}}$ are the noise standard deviation maps of each image, and $\mathcal{R}$ is a regularization metric for the phase.
Any aberration $\boldsymbol{\phi}$ is expanded on a basis $\{\boldsymbol{Z}_k\}$ that is typically either Zernike polynomials or the pixel indicator functions in the corresponding pupil plane: $\boldsymbol{\phi} = \sum_k a_k \boldsymbol{Z}_k$ where the summation is, in practice, limited to the number of coefficients considered sufficient to correctly describe the aberrations. In this paper, the phase is expanded on a truncated Zernike basis. The impact of using a regularization metric with such a basis is studied later in this paper. In the MAP framework, the regularization metrics $\mathcal{R}(\boldsymbol{\phi}_u)$ and $\mathcal{R}(\boldsymbol{\phi}_d)$ are deduced from the assumed *a priori* statistics of $\boldsymbol{\phi}_u$ and $\boldsymbol{\phi}_d$. Assuming these aberrations are zero-mean, Gaussian, and neglecting *a priori* correlations between Zernike modes, we obtain, for an estimation performed on N Zernike modes:

$$\mathcal{R}(\boldsymbol{\phi}_x) = \frac{1}{2}\boldsymbol{a}_x^t R_{a_x}^{-1} \boldsymbol{a}_x = \frac{1}{2}\sum_{k=1}^{N} \frac{a_{x_k}^2}{\sigma_{x_k}^2}, \tag{4}$$

where $\sigma_{x_k}^2$ is the assumed phase variance per Zernike mode, R_{a_k} the covariance matrix, and $\boldsymbol{a}_x$ a N element vector containing the estimated Zernike coefficients a_{x_k}. Here x is either u (upstream) or d (downstream).
The minimization of metric $J(\alpha, \beta, \boldsymbol{\phi}_u, \boldsymbol{\phi}_d)$ of Eq.(3) is performed by means of a limited memory variable metric (BFGS) method (Press et al. (2007), Thiébaut (2002)), which is a fast quasi-Newton type minimization method. It uses both gradients $\frac{\partial J}{\partial \boldsymbol{\phi}_u}$ and $\frac{\partial J}{\partial \boldsymbol{\phi}_d}$. Flux α and offset β are analytically obtained using gradients $\frac{\partial J}{\partial \alpha}$ and $\frac{\partial J}{\partial \beta}$ (implementation details, including gradient expressions, can be found in Appendix A).

Sauvage et al. (2012) established that a suitable diversity phase $\boldsymbol{\phi}_{div}$ for COFFEE was a mix of defocus and astigmatism: $\boldsymbol{\phi}_{div} = a_4^{div}\boldsymbol{Z}_4 + a_5^{div}\boldsymbol{Z}_5$ with $a_4^{div} = a_5^{div} = 80$ nm RMS, introduced upstream of the coronagraph. We therefore use this diversity phase in the following.

2.2. Coronagraphic imaging model

The imaging model used by COFFEE in the criterion minimization (equation (3)) requires a coronagraphic PSF expression. In this paper, we use the analytical coronagraphic imaging model developed by Sauvage et al. (2010), whose formalism is developed in this section, where $\boldsymbol{r}$ is the pupil plane position vector, r its modulus, and $\boldsymbol{\gamma}$ the focal plane position vector. The entrance pupil function $\boldsymbol{P}_u(\boldsymbol{r})$ is such that:

$$\boldsymbol{P}_u(\boldsymbol{r}) = \boldsymbol{\Pi}\left(\frac{2r}{D_u}\right)\boldsymbol{\Phi}(\boldsymbol{r}) \tag{5}$$

with $\boldsymbol{\Pi}\left(\frac{2r}{D_u}\right) = 1$ for $r \leq \frac{D_u}{2}$, pupil entrance diameter, 0 otherwise, and $\boldsymbol{\Phi}$ is an apodization function. In this paper,

we consider that the impact of amplitude aberrations is negligible, which is a reasonable assumption for a ground-based, high-contrast imaging system such as SPHERE. Considering only static aberrations (no residual turbulent aberrations), the electric field $\boldsymbol{\Psi}_A$ in the entrance pupil plane can be written as

$$\boldsymbol{\Psi}_A(\boldsymbol{r}) = \boldsymbol{P}_u(\boldsymbol{r})e^{j\boldsymbol{\phi}_u(\boldsymbol{r})}, \tag{6}$$

The field amplitude $\boldsymbol{\Psi}_B(\boldsymbol{\gamma})$ in plane B can be calculated, following Sauvage et al. (2010), using the analytical coronagraphic imaging model (which is called "perfect coronagraph model" hereafter):

$$\boldsymbol{\Psi}_B(\boldsymbol{\gamma}) = \mathrm{FT}^{-1}(\boldsymbol{\Psi}_A(\boldsymbol{r})) - \eta_0 \mathrm{FT}^{-1}(\boldsymbol{P}_u(\boldsymbol{r})), \tag{7}$$

where η_0 is the scalar that minimizes the outcoming energy from focal plane B, whose analytical value is given by

$$\eta_0 = \frac{1}{\mathcal{N}} \iint_S \boldsymbol{\Psi}_A^*(\boldsymbol{r})\boldsymbol{P}_u(\boldsymbol{r})d\boldsymbol{r}, \tag{8}$$

where

$$\mathcal{N} = \iint_S \boldsymbol{P}_u^*(\boldsymbol{r})\boldsymbol{P}_u(\boldsymbol{r})d\boldsymbol{r}. \tag{9}$$

It is worthy mentioning that η_0 is the exact definition of the instantaneous Strehl ratio given by Born & Wolf (1989). One can notice that $\eta_0 = 1$ when there is no aberration upstream of the coronagraph ($\boldsymbol{\phi}_u(\boldsymbol{r}) = 0$), so that $\boldsymbol{\Psi}_B = 0$ in such a case. No aberration in the entrance pupil leads to no outcoming energy from plane B, and thus to a perfect extinction in the detector plane D.
Propagating the wave from plane B (Eq. (7)) to plane D, we can write the electric field $\boldsymbol{\Psi}_D(\boldsymbol{\gamma})$ in the detector plane:

$$\begin{aligned}\boldsymbol{\Psi}_D(\boldsymbol{\gamma}) =& \mathrm{FT}^{-1}\left\{\boldsymbol{P}_d(\boldsymbol{r})e^{j(\boldsymbol{\phi}_u(\boldsymbol{r})+\boldsymbol{\phi}_d(\boldsymbol{r}))}\right\} \\ &- \eta_0 \mathrm{FT}^{-1}\left\{\boldsymbol{P}_d(\boldsymbol{r})e^{j\boldsymbol{\phi}_d(\boldsymbol{r})}\right\},\end{aligned} \tag{10}$$

where $\boldsymbol{P}_d(\boldsymbol{r})$ is the Lyot stop pupil function: $\boldsymbol{P}_d(\boldsymbol{r}) = \boldsymbol{\Pi}\left(\frac{2r}{D_d}\right)\boldsymbol{P}_u(\boldsymbol{r})$, with D_d the Lyot stop pupil diameter ($D_d \leq D_u$). For the sake of simplicity, we omit the spatial variables $\boldsymbol{r}$ and $\boldsymbol{\gamma}$ in the following. The coronagraphic PSF of the instrument, denoted by $\boldsymbol{h}_c$, is the square modulus of $\boldsymbol{\Psi}_D$:

$$\begin{aligned}\boldsymbol{h}_c(\boldsymbol{\phi}_u, \boldsymbol{\phi}_d) =& \left|\mathrm{FT}^{-1}(\boldsymbol{P}_d e^{j(\boldsymbol{\phi}_u+\boldsymbol{\phi}_d)})\right. \\ &\left. - \eta_0 \mathrm{FT}^{-1}(\boldsymbol{P}_d e^{j\boldsymbol{\phi}_d})\right|^2.\end{aligned} \tag{11}$$

In this paper, this expression of the coronagraphic PSF is the one used by COFFEE for estimating $\boldsymbol{\phi}_u$ and $\boldsymbol{\phi}_d$; i.e., Eq. (11) is inserted into the imaging model (Eq. (1)) used in the criterion minimization described in Eq. (3).
As described by Sauvage et al. (2010), this model, which analytically describes the impact of a coronagraph in an imaging system, considers that the coronagraph removes the projection of the incoming electric field on an Airy pattern, represented by the parameter η_0 (Eq. (8)). Since it does not assume small aberrations, it can be used for any wave-front error upstream of the coronagraph. The quality of the fit of this analytical imaging model with the ARPM coronagraph is discussed later in this paper (Section 3.5).

Simulation	
image size	$93 \times 93\ \frac{\lambda}{D}$ (128×128 pixels, oversampling factor: 1.38)
Light spectrum	monochromatic ($\lambda = 635$ nm)
Aberration upstream of the coronagraph ($\boldsymbol{\phi}_u$)	WFE = 80 nm RMS
Aberration downstream of the coronagraph ($\boldsymbol{\phi}_d$)	WFE = 20 nm RMS
Zernike basis used for $\boldsymbol{\phi}_u$ and $\boldsymbol{\phi}_d$ simulation	36 Zernike polynomials
Phase estimation: COFFEE	
Zernike basis used for $\boldsymbol{\phi}_u$ and $\boldsymbol{\phi}_d$ reconstruction	36 Zernike polynomials
Regularization metric	none

Table 1. COFFEE: simulation parameters used for the performance assessments of sections 3.1, 3.2 and 3.3

3. Performance assessment by numerical simulation

The aim of this section is to quantify the impact of each error source on COFFEE's aberration estimation. Such a study will show COFFEE's sensitivity to the classical error sources that limit the phase retrieval in a real system (and thus the final extinction of the coronagraph), which will be of high interest in defining COFFEE's upgrades. Likewise, it will allow us to estimate the accuracy level expected on our AO bench. In this section, we present the evolution of this reconstruction error with respect to the incoming flux (Section 3.1), to the size of the source (Section 3.2), to an error made on the assumed diversity phase used in the reconstruction (Section 3.3), and to the number of Zernike modes used in the reconstruction (Section 3.4). For each error source, coronagraphic images will be computed using the imaging model presented in Eq. (1), using the perfect coronagraph model to calculate the coronagraphic PSF h_c whose expression is given Eq. (11). COFFEE will then perform the phase estimation using these two images. The compatibility of COFFEE with realistic coronagraphic images will be studied as well (Section 3.5) by computing coronagraphic images using a realistic coronagraph model and then running COFFEE to estimate the aberrations both upstream and downstream of the coronagraph.
Table 1 gathers the parameters used for these simulations.

The chosen wave-front error (WFE) values upstream and downstream of the coronagraph for these simulations are typical of the aberrations that will be estimated on our AO bench in Section 4 (so that experimental results can be compared to the following simulations). Since these simulations are performed with a small number of Zernike modes (36), there is no need of regularization metrics in such simulations.
To simulate realistic aberrations, we have considered that the variance per Zernike mode σ_k^2 was decreasing with the radial order $n(k)$ of the considered Zernike mode k (Noll (1976)):

$$\sigma_k^2 \propto \frac{1}{n(k)^2}\,. \tag{12}$$

This corresponds to a decrease in the static aberration spatial spectrum as $\frac{1}{|\nu|^2}$, where ν is the spatial frequency, which is a common assumption for mirror fabrication errors. To evaluate COFFEE's performance, we define the reconstruction error ϵ_x

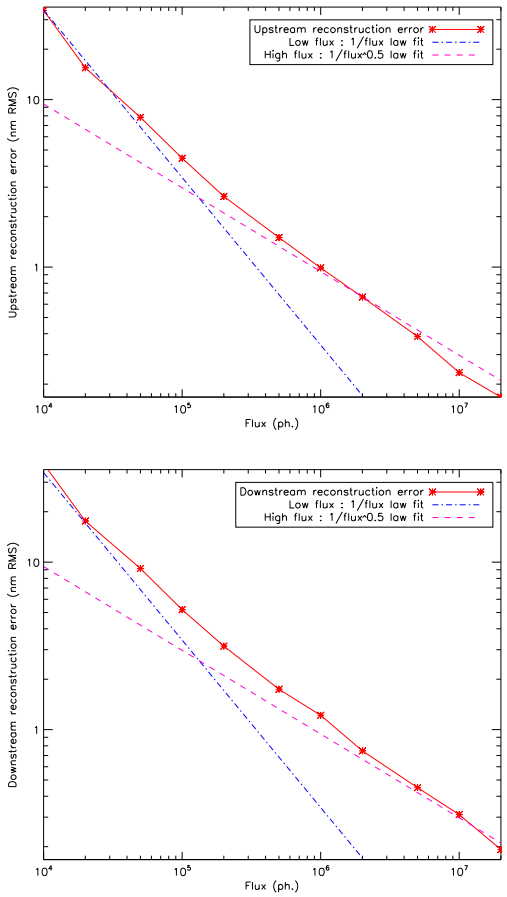

Fig. 2. Aberrations upstream (ϕ_u (WFE $= 80$ nm), top) and downstream (ϕ_d (WFE $= 20$ nm), bottom) of the coronagraph: reconstruction error (solid red line) as a function of the incoming flux α. For comparison, $\frac{1}{\alpha}$ (cyan dashed line) and $\frac{1}{\sqrt{\alpha}}$ (magenta dashed line) theoretical behaviours are plotted for detector noise only and photon noise only (respectively).

(x stands for u (upstream) or d (downstream)) as

$$\epsilon = \sqrt{\sum_{k=2}^{N-1} |a_k - \hat{a}_k|^2} \tag{13}$$

with a_k the Zernike coefficients (starting with $k = 2$ corresponding to tilt) used for the simulation, $\hat{a}_k$ the reconstructed Zernike coefficients, and N the number of Zernike modes. In this section, every reconstruction error value is an average value, computed from ten independent simulated phases.

3.1. Noise propagation

The ultimate limitation of an instrument lies in the amount of noise in the images. In Figure 2, we present the reconstruction error for the aberrations upstream (ϕ_u) and downstream (ϕ_d) of the coronagraph with respect to the total incoming flux. Photon noise and detector noise ($\sigma_{\text{det}} = 6$ e$^-$) are added in the coronagraphic images for simulation.

The evolution of the reconstruction error presented in Figure 2 is proportional to $(1/\alpha)$ for the detector noise limited regime (low flux) and to $(1/\sqrt{\alpha})$ for the photon noise limited regime (high flux). In this figure, it can be seen that for an incoming flux $\alpha \geq 10^6$ photons, the reconstruction error ϵ_u for the phase upstream of the coronagraph is smaller than 1 nm RMS. Thus, in a calibration process, where high values of flux ($\geq 10^6$ photons) can be easily reached, COFFEE's performance will not be significantly affected by noise.

It is noteworthy that the results of many similar simulations with various levels of upstream aberrations show that COFFEE's reconstruction error does not depend on the amplitude of the aberrations upstream of the coronagraph, as long as the diversity phase amplitude is larger than the WFE of the aberrations to be estimated.

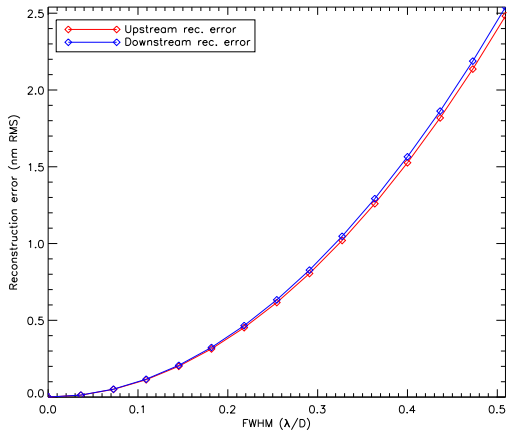

Fig. 3. Error reconstructions upstream (red line) and downstream (blue line) of the coronagraph as functions of the size of the source on the coronagraph.

3.2. Impact of the source size on the reconstruction error

Our imaging model, presented in Section 2.1 (Eq. 1), assumes an unresolved object. Thus, the presence of a real source with a given spatial extension will have an impact on the phase reconstruction, which is quantified here. We consider here a Gaussian-shaped laser source, emitted from a single-mode fiber. Because of the incoming light coherence, it can be represented as a Gaussian amplitude in the entrance pupil plane (where COFFEE assumes a uniform amplitude). Knowing this, coronagraphic images are simulated by considering a small coherent Gaussian-shaped beam (FWHM $\leq 0.5\frac{\lambda}{D}$) on the coronagraph, and then processed by COFFEE.

Since the imaging model assumes an unresolved object, both reconstruction errors for the phases upstream and downstream of the coronagraph increase with the FWHM of the coherent object, as showed in Figure 3, but remains low: for an FWHM smaller than $\frac{\lambda}{3D}$, the reconstruction error is indeed sub-nanometric. The size of the laser source will thus definitely not be a limitation for COFFEE: if this error is not negligible in the total error budget, it is possible to include it in the imaging model used by COFFEE (Eq. 1) as a non-uniform (Gaussian) entrance pupil function $\boldsymbol{P}_u(\boldsymbol{r})$.

3.3. Sensitivity to a diversity phase error

The diversity phase $\boldsymbol{\phi}_{div} = a_4^{div}\boldsymbol{Z}_4 + a_5^{div}\boldsymbol{Z}_5$ has been defined in Section 2.1. This phase $\boldsymbol{\phi}_{div}$ is one of the inputs that COFFEE needs in order to perform phase retrieval, so it must be calibrated as accurately as possible. To optimize the use of COFFEE, the impact of an error on such a calibration is studied. In this section, we consider that the diversity phase used to

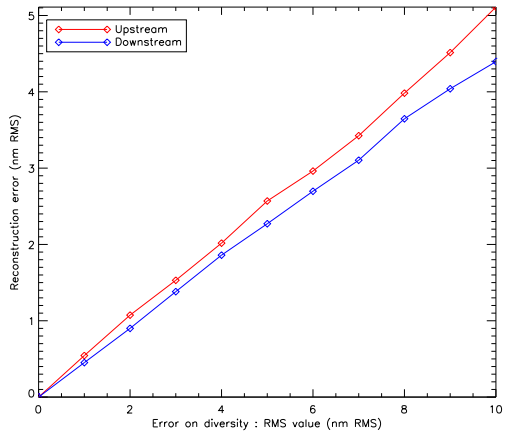

Fig. 4. Error reconstructions upstream (solid red line) and downstream (solid blue line) of the coronagraph as functions of the error on the diversity phase.

Simulation	
image size	93×93 $\frac{\lambda}{D}$ (128×128 pixels, oversampling factor: 1.38)
Light spectrum	monochromatic ($\lambda = 635$ nm)
Aberration upstream of the coronagraph (ϕ_u)	WFE $= 80$ nm RMS
Aberration downstream of the coronagraph (ϕ_d)	WFE $= 20$ nm RMS
Zernike basis used for ϕ_u and ϕ_d simulation	350 Zernike polynomials
Incoming flux	$5\ 10^6$ photons
noise	photon noise, detector noise ($\sigma_{\text{det}} = 1$ e$^-$)
COFFEE: phase estimation	
Zernike basis used for ϕ_u and ϕ_d reconstruction	from 15 to 275 Zernike polynomials
Regularization metric	With and without

Table 2. COFFEE: simulation parameters for studying the aliasing error.

create the diversity image is not perfectly known. The coronagraphic simulated diversity image is computed with a diversity phase $\phi'_{div} = \phi_{div} + \phi_{err}$, with ϕ_{err} a randomly generated phase of given RMS value, and COFFEE's phase reconstruction is done considering that the diversity phase is equal to ϕ_{div}. In Figure 4, we see that the reconstruction error increases linearly with the calibration error on the diversity phase, with a slope of 0.5. Thus, the requirement on the calibration precision for the diversity phase is typically the precision wanted for the aberration measurement.

3.4. Impact of aliasing

The phase estimation is performed here on a truncated Zernike basis. In real images (recorded from a bench), some speckles will originate in high-order aberrations. These aberrations, which cannot be fitted by the truncated Zernike basis, will have an impact on the phase estimation, called aliasing error hereafter. Thus, it is necessary to study this aliasing error as a function of the number of Zernike modes used in the phase reconstruction. Here, we generate a phase on a large number of Zernike modes, and compute the corresponding images using the perfect coronagraph model. Aberrations both upstream and downstream of the coronagraph are then estimated by COFFEE using an increasing number of Zernike modes. Since one of the aims of this simulation is to determine the size of the truncated Zernike basis to be used with experimental data recorded on an in-house bench, the noise level in the simulated images corresponds to the one we have on this bench. The total incoming flux is $5\ 10^6$ photons, and the detector noise is $\sigma_{\text{det}} = 1$ e$^-$ per pixel. Parameters used for this simulation are gathered in Table 2. This simulation has been done with and without a regularization metric, so that we can demonstrate the relevance of this metric on phase estimation.

Figure 5 presents the evolution of the reconstruction errors when the number of reconstructed Zernike modes increases. Here, every reconstruction error (Eq. (13)) is calculated on a basis of 350 Zernike modes; thus, the error originates both in high-order aberrations, which are not considered by COFFEE because of the Zernike basis finite size (modelling error), and in the impact of these high-order aberrations on the estimated ones (aliasing). The WFE corresponding to the aberrations that are not estimated by COFFEE (from N to 350, where N varies between 15 and 275 according to Table 2) is called "unmodelled WFE" hereafter.

In the plot of the reconstruction error upstream of the coronagraph evolution (Figure 5, top), one can see that without a regularization metric, the reconstruction error increases for a large number of Zernike modes. An interpretation of this behaviour is the following: because high-order aberrations have a smaller variance, their associated speckle intensity is lower. Thus, owing to the photon and detector noise in the image, the SNR is smaller for these aberrations. Such behaviour leads to a trade-off between aliasing and noise amplification for the optimal number of Zernike modes (Figure 5). The best number of Zernike modes is then a function of the aberrations level (WFE) and spectrum, as well as of the level of noise. The use of a regularization metric allows us to avoid this noise amplification (Figure 5): the reconstruction error roughly reaches a saturation level (rather than growing to very high values). Additionally, the use of regularization reduces the aliasing error, and avoids the need for the difficult and somewhat *ad hoc* choice of number of Zernike modes for the reconstruction.

According to the results presented in Figure 5, we have chosen to estimate the aberrations upstream and downstream of the coronagraph on 170 Zernike modes with the regularization metric of Eq. (4).

3.5. Model mismatch

We have already demonstrated that ARPM images are compatible with the perfect coronagraph model and therefore with COFFEE estimation in Sauvage et al. (2012). The Roddier & Roddier Phase Mask (RRPM) (Roddier & Roddier (1997), Guyon et al. (1999)) consists in a π phase shifting mask slightly smaller than the Airy disk. Additionally, the use of a circular prolate function as entrance pupil apodization $\mathbf{\Phi}_P$ (ARPM), proposed by Soummer et al. (2003), leads in a perfect case (no aberrations upstream of the coronagraph) to a total suppression of signal in the detector plane. In the simulations presented hereafter, realistic ARPM coronagraphic images are computed following Soummer et al. (2007) to consider an accurate numerical representation of Lyot-style coronagraphs. Then, we use

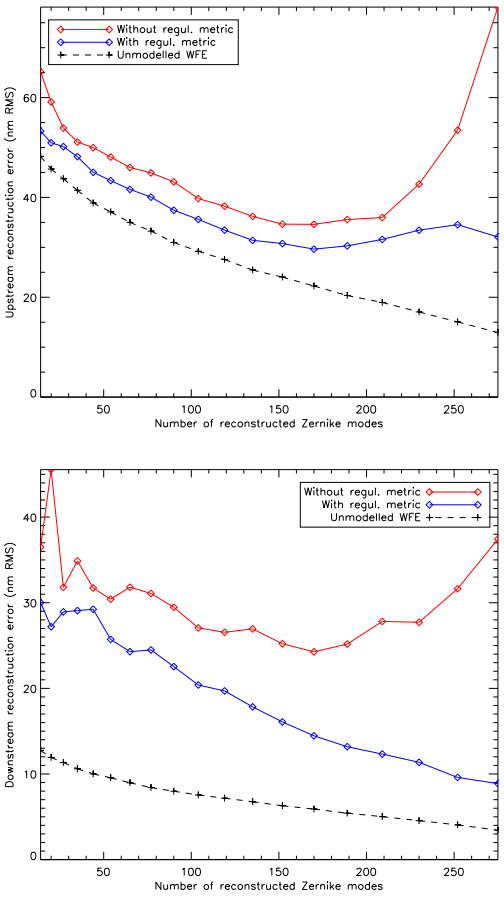

Fig. 5. Error reconstructions upstream (top) and downstream (bottom) of the coronagraph as functions of the number of reconstructed Zernike modes, with a regularization metric (solid blue line) and without (solid red line)

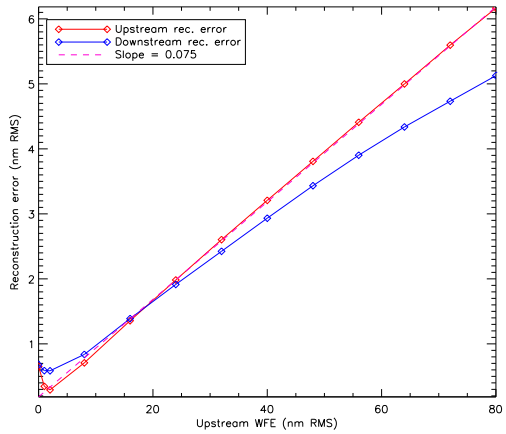

Fig. 6. Error reconstruction upstream of the coronagraph with respect to the WFE of the aberration upstream of the coronagraph

COFFEE to reconstruct both phases upstream and downstream of the coronagraph. Here, when using the formalism developed in Section 2.2, the prolate apodization function $\mathbf{\Phi}_P$ is included in both simulation and reconstruction imaging models.

Because the perfect coronagraph model is not exactly identical to an ARPM (although their responses to aberrations

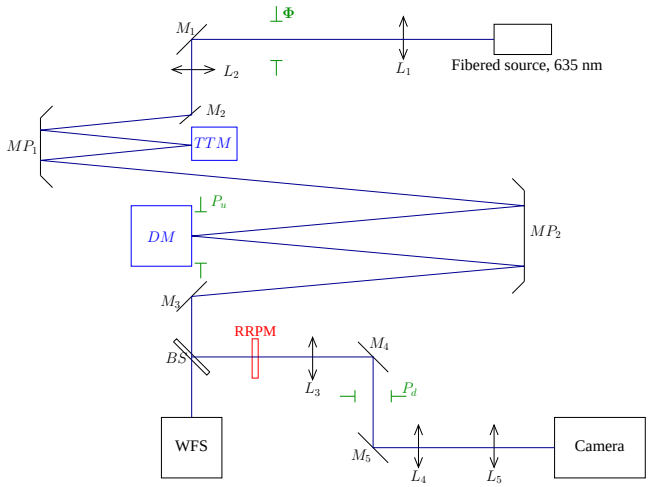

Fig. 7. Adaptive optics testbed schematic representation. M_i: fold mirrors; MP_i: parabolic mirrors; L_i: lenses (doublets); BS: beam splitter; TTM: Tip-Tilt mirror; DM: Deformable mirror; RRPM: coronagraphic focal plane mask; $\mathbf{\Phi}$: prolate apodizer; WFS: AO wave-front sensor

is very close), there is a model mismatch in the estimation of aberrations upstream of the coronagraph ϕ_u, which varies linearly with the WFE of ϕ_u, as shown in Figure 6. The model mismatch can thus be quantified as 7.5% of the WFE RMS value of ϕ_u, except for very small WFE (≤ 1 nm RMS), where the variation is non-linear, but remains below 1 nm RMS.
Since the variation in this model mismatch varies linearly with the WFE of ϕ_u, it should not limit the ability to compensate for the aberration upstream of an ARPM using COFFEE as focal plane wave-front sensor (WFS).

4. Laboratory demonstration

In this section we present experimental validations in the coronagraphic phase diversity. These validations are done on the bench BOA, described in Section 4.1. Section 4.2 describes a carefully designed method developed to introduce calibrated static aberrations on the AO bench to be measured with COFFEE. The error made on the measurements of aberrations upstream of the coronagraph (NCPA) is quantified in Section 4.3. Section 4.4 presents the static aberration measurement performance, and Section 4.5 details the procedure for compensating for the measured aberrations.

4.1. Experimental setup

Figure 7 shows the design of our in-house bench. The input beam, emitted from a fibered laser source ($\lambda = 635$ nm) comes through the prolate apodizer $\mathbf{\Phi}$, which is in the entrance pupil plane (P_u). The beam is reflected by the tip-tilt mirror (TTM) and then by the deformable mirror (DM, entrance pupil, $D_u = 40$ mm, 6×6 actuators). The beam-splitter sends a fraction of the beam to the AO wave-front sensor (Shack-Hartmann, 5×5 sub-apertures). On the other channel, the light is focused onto a RRPM, whose diameter is $d_c = 18.1$ μm (angular diameter is $1.06\frac{\lambda}{D_u}$). After going through the Lyot stop plane (P_d, with $D_d = 0.99 D_u$), the beam is focused onto the camera (256×256 pixels images with an oversampling of 2.75, detector noise $\sigma_{\text{det}} = 1$ e$^-$). For faster computations, recorded images are rebinned to 128×128 pixels images with an oversampling of 1.38.

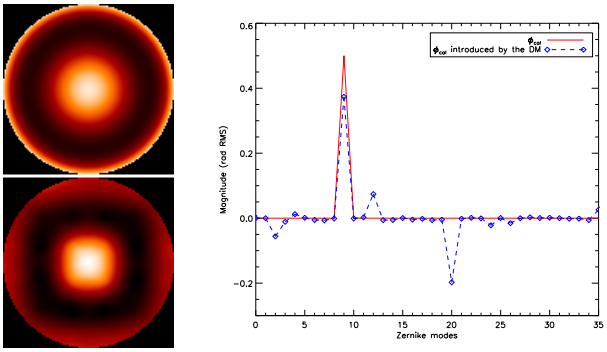

Fig. 8. Introduction of calibrated aberration on BOA: case of a pure spherical aberration. Left: theoretical wave-front (top) and DM introduced wave-front (bottom). Right: corresponding Zernike modes for the theoretical introduced aberration (solid red line) and the DM introduced aberration (dashed blue line).

4.2. Introduction of calibrated aberrations

To evaluate COFFEE's performance, we introduce calibrated aberrations on the bench using a process described in this section. We consider an aberration phase $\boldsymbol{\phi}_{cal}$ to be introduced on BOA. First, since the phase is represented by the DM with a finite number of actuators (6×6), the introduced aberration will not match the aberration $\boldsymbol{\phi}_{cal}$ perfectly, as illustrated in Figure 8 in the case of a pure spherical aberration.

Our aim is here to introduce, using the DM, the closest aberration to the aberration $\boldsymbol{\phi}_{cal}$. We let $\boldsymbol{F}$ be the DM influence matrix (obtained by calibration); any DM introduced aberration $\boldsymbol{\phi}^{DM}$ can be described as a set of actuator voltages $\boldsymbol{u}$ ($\boldsymbol{\phi}^{DM} = \boldsymbol{F}\boldsymbol{u}$). We are thus looking for the set $\boldsymbol{u}_{cal}$ which solves the least-squares problem:

$$\boldsymbol{u}_{cal} = \arg\min_{\boldsymbol{u}} \|\boldsymbol{F}\boldsymbol{u} - \boldsymbol{\phi}_{cal}\|^2 . \tag{14}$$

The solution of this problem can be written as

$$\boldsymbol{u}_{cal} = \boldsymbol{T}\boldsymbol{\phi}_{cal}, \tag{15}$$

with $\boldsymbol{T}$ the generalized inverse of matrix $\boldsymbol{F}$. Using the interaction matrix $\boldsymbol{D}$ (resulting from calibration), we can compute the corresponding set of slopes $\boldsymbol{s}_{cal}$ ($\boldsymbol{s}_{cal} = \boldsymbol{D}\boldsymbol{u}_{cal}$), which can then be used to modify the AO loop reference slopes $\boldsymbol{s}_{\text{ref}}$. Thus, closing the AO loop with the reference slopes $\boldsymbol{s}_{\text{ref}} + \boldsymbol{s}_{cal}$, we introduce an aberration $\boldsymbol{\phi}_{cal}^{DM} = \boldsymbol{F}\boldsymbol{u}_{cal} = \boldsymbol{F}\boldsymbol{T}\boldsymbol{\phi}_{cal}$ on the bench, which is the best fit of $\boldsymbol{\phi}_{cal}$ in the least squares sense.
We also have to consider that the bench BOA presents its own unknown static aberrations $\boldsymbol{\phi}_u^{\text{BOA}}$ and $\boldsymbol{\phi}_d^{\text{BOA}}$ upstream and downstream of the coronagraph (respectively). Thus, if a calibrated aberration $\boldsymbol{\phi}_{cal}$ is introduced in the entrance pupil, aberrations $\boldsymbol{\phi}_u$ upstream of the coronagraph will be

$$\boldsymbol{\phi}_u = \boldsymbol{\phi}_{cal} + \boldsymbol{\phi}_u^{\text{BOA}}. \tag{16}$$

To get rid of the unknown aberration $\boldsymbol{\phi}_u^{\text{BOA}}$, we perform a differential phase estimation:

1. We introduce the aberration $\boldsymbol{\phi}_{cal}^{DM}$ on the bench. A phase $\hat{\boldsymbol{\phi}}_u^{+} = \hat{\boldsymbol{\phi}}_{cal}^{DM} + \hat{\boldsymbol{\phi}}_u^{BOA}$ is estimated using focused and diverse images recorded on the camera.
2. The opposite aberration $-\boldsymbol{\phi}_{cal}^{DM}$ is then introduced. A phase $\hat{\boldsymbol{\phi}}_u^{-} = -\hat{\boldsymbol{\phi}}_{cal}^{DM} + \hat{\boldsymbol{\phi}}_u^{BOA}$ is estimated.
3. The half difference $\hat{\boldsymbol{\phi}}_{cal}^{DM} = \frac{\hat{\boldsymbol{\phi}}_u^{+} - \hat{\boldsymbol{\phi}}_u^{-}}{2}$ is our estimate of $\boldsymbol{\phi}_{cal}$.

The first use of this process is to calibrate the diversity phase itself. Since this phase will be introduced using the AO system, the actually introduced diversity phase will not exactly match the theoretical mix of defocus and astigmatism. We introduce the aberrations $\boldsymbol{\phi}_{div}$ and $-\boldsymbol{\phi}_{div}$ on the bench using the AO system. These two aberrations are then estimated using classical phase diversity (no coronagraph), with a pure defocus of diversity phase introduced using a flat glass plate of known thickness e in a focused beam.
Such a process gives us an accurate estimation of the diversity phase really introduced on the bench, with an estimated accuracy of 4 nm RMS on the introduced aberration. This calibration is then used in COFFEE's estimations performed on experimental images.

4.3. Performance assessment: error budget

From simulations presented in Section 3, we establish an error budget for estimating aberrations upstream of the coronagraph using experimental data:

- ◇ Photon and detector noise error: on the BOA bench, the typical incoming flux is $f_{\text{BOA}} = 5\ 10^6$ photons. Knowing that we have photon noise and a detector noise with $\sigma_{\text{det}} = 1$ e$^-$, we can evaluate the noise error: $\epsilon_{\text{noise}} = 0.9$ nm RMS.
- ◇ The diversity phase $\boldsymbol{\phi}_{div}$ has been calibrated using classical phase diversity, using the process presented in Section 4.2. Such an estimation has been performed with an error of 4.0 nm RMS (value calculated from an error budget evaluated for a classical phase diversity estimation on the BOA bench. Such accuracy has already been obtained on this bench by Sauvage et al. (2007)). According to Section 3.3, this error on the diversity phase leads to an error $\epsilon_{\text{model}} = 2.0$ nm RMS.
- ◇ The source is a coherent Gaussian-shaped beam whose FWHM is $0.27\frac{\lambda}{D}$ on the coronagraph. According to the simulations of Section 3.2, this leads to a reconstruction error: $\epsilon_{\text{obj}} = 0.7$ nm RMS.
- ◇ Residual turbulent speckles, which originate in uncorrected turbulent aberrations, are not included in the imaging model. To measure the impact of these speckle on the reconstruction, several wave-fronts have been successively recorded using a commercial Shack-Hartmann wave-front sensor. From these acquisitions, we calculate the WFE of the residual turbulent phase: $\sigma_{\phi_{\text{turb}}} = 1.2$ nm RMS. This residual turbulence will create speckles on the detector, which will be considered by COFFEE as originating in NCPA. Thus, the residual turbulence error ϵ_{turb} made by COFFEE is estimated to $\epsilon_{\text{turb}} = \sigma_{\phi_{\text{turb}}} = 1.2$ nm RMS.
- ◇ Aliasing error, which originates in high-order aberrations, has been studied in Section 3.4. For a phase upstream of the coronagraph estimated on $N = 170$ Zernike modes, we have $\epsilon_{\text{aliasing}} = 18.3$ nm RMS.
- ◇ From simulations, we know that the model mismatch is 7.5% of WFE. For this study, we will not estimate aberrations with a WFE stronger than 80 nm RMS. For such a WFE, the model error is $\epsilon_{\text{model}} = 6.0$ nm RMS.

As one can see in Table 3, the error budget is mainly driven by the aliasing error. The second most important term is the model mismatch (even though it goes to zero with the WFE).

Error budget	
Noise	$\epsilon_{\text{noise}} = 0.9$ nm RMS
Model mismatch	$\epsilon_{\text{model}} = 6.0$ nm RMS
Error on diversity	$\epsilon_{\text{div}} = 2.0$ nm RMS
Resolved object	$\epsilon_{\text{obj}} = 0.7$ nm RMS
Residual turbulence	$\epsilon_{\text{turb}} = 1.2$ nm RMS
Aliasing	$\epsilon_{\text{aliasing}} = 18.3$ nm RMS
Total error	$\epsilon = \sqrt{\sum_i \epsilon_i^2} = 20.6$ nm RMS
Total error per Zernike mode	$\epsilon' = 1.6$ nm RMS per estimated Zernike mode

Table 3. COFFEE: error budget for the estimation of an aberration upstream of the coronagraph on BOA.

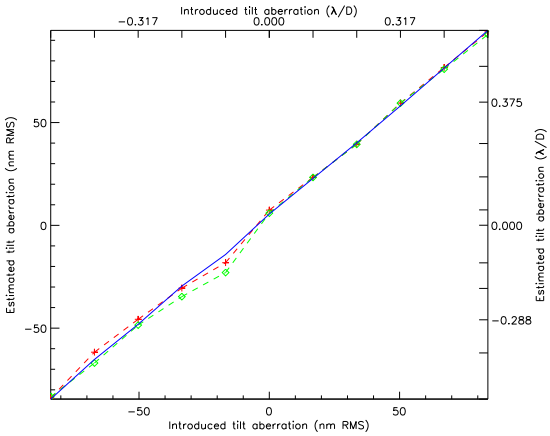

Fig. 9. Estimation of a tilt aberration on BOA: calibration (solid blue line) and COFFEE's estimation with bound on the tip-tilt downstream of the coronagraph (dashed crossed red line) and without boundaries (dashed diamond green line)

4.4. Measurement of aberrations upstream of the coronagraph

In this section, we introduce calibrated aberrations on the BOA bench upstream of the coronagraph, and then estimate them with COFFEE in order to evaluate its performance. In the course of this study, we realized that the position of the coronagraphic image on the detector (quantified by the tip-tilt downstream of the coronagraph) is a critical issue. Indeed, it occurred that COFFEE was able to perform phase retrieval only for downstream tip-tilt $[a_2, a_3]$ values within the range $[-100 \text{ nm RMS}; 100 \text{ nm RMS}]$ ($[-\frac{\lambda}{6D}; \frac{\lambda}{6D}]$). To get rid of this constraint, we have developed a method to perform a preliminary estimation of the tip-tilt downstream of the coronagraph. This method, which uses the diversity image, is fully described in Appendix B.

4.4.1. Measurement of tip-tilt upstream of the coronagraph

We present the estimation of a tilt aberration upstream of the coronagraph using COFFEE in this section. Using the AO system, we introduce a tilt aberration by adding a constant value $\delta \boldsymbol{s}_{\text{TT}}$ to the AO wave-front sensor references slopes s_{ref}, and then closing the AO loop on the slopes $\boldsymbol{s}_{\text{ref}} + \delta \boldsymbol{s}_{\text{TT}}$. To accurately calibrate the introduced tilt, for each position, we first estimate the aberrations using classical phase diversity (no coronagraph). Then, the RRPM is put in the focal plane, and the same operation is repeated: for each position, we record two images, and then estimate the aberrations using COFFEE.

From the upstream tilt reconstruction performed by COFFEE (Figure 9), we calculate an average reconstruction error: $\epsilon_{\text{tilt}} = 2.1$ nm. Part of this error is due to an error on the estimation of tip-tilt downstream of the coronagraph. An improved estimation has been performed by setting boundaries on the downstream tip-tilt. Its value is evaluated before COFFEE's estimation using the method described in appendix B with the diversity coronagraphic image recorded for a tip-tilt upstream the coronagraph value close to 0 nm RMS (centered coronagraph). Such an estimation process gives us an estimation of tip-tilt downstream of the coronagraph $\{a_2^{\text{do}}, a_3^{\text{do}}\}$ with an accuracy of ± 1.5 nm RMS. Using this estimation as the starting value for the minimization, and setting bounds of ± 1.5 nm RMS on it, we processed the same experimental data. This, in turn, results in a better estimation of tilt upstream of the coronagraph (Figure 9), with an average error $\epsilon_{\text{tilt}} = 1.5$ nm, which is close to the expected error per Zernike mode given in Section 4.3 ($\epsilon' = 1.6$ nm RMS).

4.4.2. NCPA measurements

In this section, we introduce aberrations upstream of the coronagraph. The aberration ϕ_{cal} is expanded on the first 15 Zernike modes (which is the largest number of modes we can properly describe with our 6×6 DM), and then we estimate these aberrations using COFFEE, following the process described in Section 4.2. To take the DM action into account on the introduced phase (illustrated in Figure 8), aberrations ϕ_{cal} are first estimated with classical phase diversity (no phase mask in the coronagraphic focal plane (Sauvage et al. (2007))). This estimation gives us a calibration of the introduced aberration, which is then used to evaluate the accuracy of COFFEE's estimation.

At convergence of the reconstruction, a very good match can be observed between the experimental images and the ones computed for the estimated aberrations (Figure 10, top and middle). This, in turn, results in a very good match between the aberrations measured by COFFEE (Figure 10, right) and the introduced ones (Figure 10, left).
From the experimental phase estimation presented in Figure 10, we compute a reconstruction error between the classical diversity phase calibrated aberration and COFFEE's estimation:

$$\epsilon_{\text{exp}} = 22.5 \text{ nm RMS}. \quad (17)$$

One can notice that this error is close to the expected error budget, i.e. that there is a good match between the performance assessment study carried out in Section 3 and the experimental results presented in this section.

4.5. Low-order NCPA compensation

Lastly, the ability of COFFEE to compensate for the aberrations upstream of the coronagraph is experimented on BOA. In Section 4.4, the aberrations upstream of the coronagraph are expanded on 170 Zernike modes, in order to have the smallest reconstruction error (according to Section 3.4).
As previously mentioned, the compensation on BOA is limited to the 15^{th} Zernike mode. Thus, what is required in a closed loop process is the most accurate estimation of 15 Zernike modes rather than an accurate measurement of every estimated Zernike mode. Using a basis of 36 Zernike modes for the reconstruction is sufficient to give an accurate estimation of the first 15

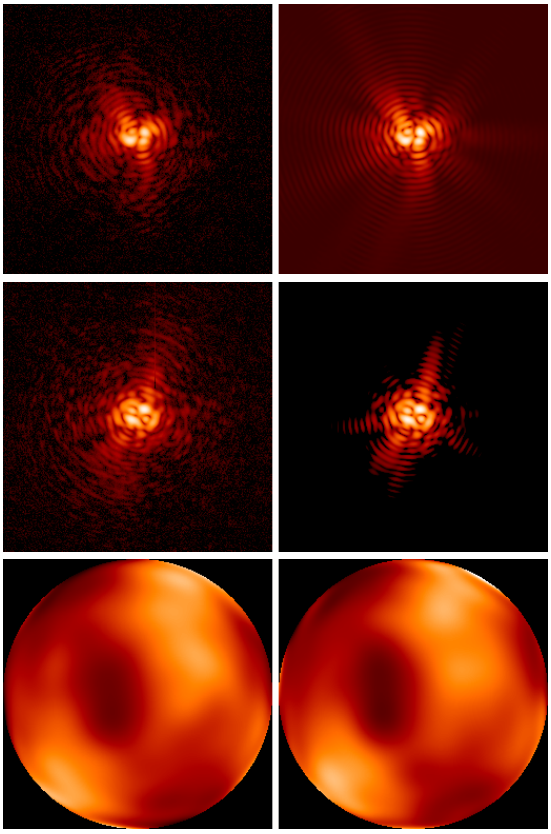

Fig. 10. COFFEE: NCPA estimation of an introduced phase ϕ_{cal} on BOA. Top: for an aberration $+\phi_{cal}$, recorded coronagraphic image from the bench (left) and computed image using the reconstructed aberration $\hat{\phi}_u^+$ (right) (log. scale, same range for both images). Middle: same images for an aberration $-\phi_{cal}$ introduced and a reconstructed aberration $\hat{\phi}_u^-$ (log. scale, same range for both images). Bottom: calibrated introduced aberration (left) and COFFEE estimated aberration (right)

Zernike modes: the aliasing error, which is the most important error source, will mainly degrade the estimation accuracy of the reconstructed high orders (close to Z_{36}).
To demonstrate the ability of COFFEE to be used in a closed loop, we introduce a set of aberrations on the DM by modifying the reference slopes, as described in Section 4.2. Then, we use the pseudo-closed loop (PCL) method described in Sauvage et al. (2007). This iterative process has two stages: for the PCL iteration i:

1. acquisition of the focused $\boldsymbol{i}_c^f$ and diverse $\boldsymbol{i}_d^f$ images;
2. estimation of the aberration $\hat{\boldsymbol{\phi}}_u^i$ upstream of the coronagraph;
3. computation of the corresponding reference slopes correction $\delta \boldsymbol{s} = g\boldsymbol{D}\boldsymbol{T}\hat{\boldsymbol{\phi}}_u^i$, where $\boldsymbol{D}$ and $\boldsymbol{T}$ are the interaction and influence matrices defined in Section 4.2 and g is the PCL gain;
4. the AO loop is closed on the modified reference slopes.

The computation time (step 2) varies from 1 minute to 2.5 minutes, allowing us to compensate for quasi-static aberrations upstream of the coronagraph. This compensation process is limited by the estimation accuracy of the first 15 Zernike modes performed by COFFEE, which corresponds to the error budget established in Section 4.3), and by the ability of the DM to reproduce a given wave-front. Indeed, the correction introduced

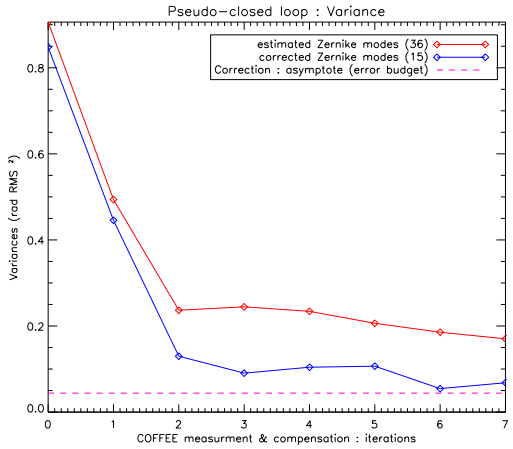

Fig. 11. PCL on the bench BOA ($g_{\mathrm{PCL}} = 0.5$): variance of the residual static aberrations upstream of the coronagraph for the 36 COFFEE estimated Zernike modes (solid red line) and the 15 corrected modes (solid blue line). The magenta dashed line represents the ultimate performance one can reach according to the error budget detailed in 4.3

on the bench (step 2 of the PCL process) is the best fit of the estimated phase $\hat{\boldsymbol{\phi}}_u^i$ in the least-square sense (as presented in Section 4.2). The difference between the estimated aberration and the actual introduced correction will thus limit the compensation performance of the PCL process. Considering these two limitations, one can compute the variance σ^2_{BOA} (for the first 15 Zernike modes) that can be reached on the BOA bench:

$$\sigma^2_{\mathrm{BOA}} = 4.4\ 10^{-2}\ \mathrm{rad\ RMS}^2. \quad (18)$$

The correction and stabilization of the NCPA variance can be seen in Figure 11. One can see that the variance of the 15 corrected Zernike modes reaches the expected asymptotic value σ^2_{BOA}. This result is the very first demonstration of COFFEE's ability to compensate for aberrations upstream of the coronagraph. A compensation at levels compatible with SPHERE or GPI-like instruments will require th using a DM with many more actuators, and working on the reduction of the dominant term of the error budget, which is aliasing.

5. Conclusion

In this paper, we have presented a thorough simulation study (Section 3) and a first experimental validation (Section 4) of the coronagraphic wave-front sensor called COFFEE, which consists mainly in the extension of the phase diversity concept to a coronagraphic imaging system. From the validation and careful performance assessment of COFFEE, we showed that COFFEE is currently limited by the aliasing error, due to high-order aberrations, which are difficult to model with a Zernike basis.
In Section 4, we presented a first experimental validation of COFFEE using an ARPM. We introduced calibrated aberrations upstream of the coronagraph (NCPA), using the AO sub-system, and estimated them with COFFEE. The accuracy we obtained on these estimation shows a very good match with our error budget. Lastly, we used COFFEE in an iterative process to perform a preliminary validation of COFFEE's ability to compensate for the aberrations upstream of the coronagraph.
Several perspectives are currently considered to optimize COFFEE: firstly, in order to minimize the impact of the aliasing error on the phase reconstruction, we plan to perform the phase reconstruction on a pixel-wise map, which is more suitable than a

truncated Zernike basis. Secondly, we would like to improve the imaging model, both to make COFFEE work with other coronagraph than the ARPM and to reduce the model error, which is currently the second most important one, even though it goes to zero with the WFE. Two solutions are considered. In the absence of residual turbulence, an accurate imaging model is obtained by propagating the electric field through each plane of the coronagraphic imaging system (Figure 1) for an arbitrary focal plane coronagraphic mask. Such a method, where no model error needs to be considered, can be used for a laboratory calibration. Alternatively, a more accurate analytical imaging model, which could include a residual turbulent aberration, can be developed. Such a model, which could include a residual turbulent aberration, will ultimately allow us to perform NCPA estimation on images from the sky. These improvements should allow us to estimate and compensate for the aberrations upstream of the coronagraph using COFFEE with a nanometric precision in a closed loop process.

A further perspective is to extend COFFEE to phase and amplitude aberration estimation, in order to create a dark hole region in the coronagraphic image.

Acknowledgements. The authors would like to thank Mamadou N'Diaye, Kjetil Dohlen and Thierry Fusco for stimulating discussions, as well as Marc Ferrari, David Mouillet and Jean-Luc Beuzit for their support, and the Région Provence-Alpes-Côte d'Azur for partial financial support of B. Paul's scholarship. This work has been partially funded by the European Commission under FP7 Grant Agreement No. 266404 Optical Infrared Coordination Network for Astronomy.

Appendix A: Implementation details

COFFEE performs a phase estimation by minimizing a criterion J whose expression is given by equation 3. To estimate $\boldsymbol{\phi}_u$ and $\boldsymbol{\phi}_d$ (expanded on a truncated Zernike basis), we need both gradients $\frac{\partial J}{\partial \boldsymbol{a}_u}$ and $\frac{\partial J}{\partial \boldsymbol{a}_d}$, where $\boldsymbol{a}_x = \{a_{x_1}, a_{x_2}, ..., a_{x_N}\}$ is a vector that contains the Zernike coefficients, for an aberration expanded on N Zernike modes (x is for u (upstream) or d (downstream)). Let us write the numerical expression of J^{foc}, using the notations defined in Section 2.1:

$$\begin{aligned} J &= \frac{1}{2}\sum_t \left| \frac{\boldsymbol{i}_c^{\text{foc}}[t] - \alpha.\boldsymbol{h}_{\text{det}}[t] \star \boldsymbol{h}_c^{\text{foc}}[t] - \beta}{\boldsymbol{\sigma}_n^{\text{foc}}[t]} \right|^2 \\ &+ \frac{1}{2}\sum_t \left| \frac{\boldsymbol{i}_c^{\text{div}}[t] - \alpha.\boldsymbol{h}_{\text{det}}[t] \star \boldsymbol{h}_c^{\text{div}}[t] - \beta}{\boldsymbol{\sigma}_n^{\text{div}}[t]} \right|^2 \\ &+ \mathcal{R}_{\boldsymbol{\phi}_u} + \mathcal{R}_{\boldsymbol{\phi}_d} \\ &= J^{\text{foc}} + J^{\text{div}} + \mathcal{R}_{\boldsymbol{\phi}_u} + \mathcal{R}_{\boldsymbol{\phi}_d}. \end{aligned} \tag{A.1}$$

With t the pixel position in the detector plane. $\boldsymbol{\sigma}_n^{\text{foc}}$ and $\boldsymbol{\sigma}_n^{\text{div}}$ are the noise variance maps. Considering the expression of J, we derive J^{foc}, and then deduce the gradients expressions of J^{div} using a trivial substitution. Expressions of the regularization terms gradients $\frac{\partial \mathcal{R}_{\boldsymbol{\phi}_x}}{\partial \boldsymbol{a}_x}$ are given by

$$\frac{\partial \mathcal{R}_{\boldsymbol{\phi}_x}}{\partial \boldsymbol{a}_x} = R_{\boldsymbol{a}_x}^{-1} \boldsymbol{a}_x. \tag{A.2}$$

The calculation of gradients $\frac{\partial J}{\partial \boldsymbol{\phi}_u}$ and $\frac{\partial J}{\partial \boldsymbol{\phi}_d}$ is done following Mugnier et al. (2001): first, we calculate the gradient of J^{f} with respect to the PSF $\boldsymbol{h}_c$:

$$\frac{\partial J^{\text{foc}}}{\partial \boldsymbol{h}_c^{\text{foc}}} = \frac{1}{{\boldsymbol{\sigma}_n^{\text{foc}}}^2}[\alpha \boldsymbol{h}_{\text{det}}(\alpha.\boldsymbol{h}_{\text{det}} \star \boldsymbol{h}_c^{\text{foc}} - \boldsymbol{i}_c^{\text{foc}})]. \tag{A.3}$$

Then, the calculation consists in derivating the gradient of the PSF $\boldsymbol{h}_c$ with respect to phases $\boldsymbol{\phi}_u[k]$ and $\boldsymbol{\phi}_d[l]$ at pixels k, l in pupils upstream and downstream of the coronagraph, respectively, and applying the chain rule, as already done in a non-coronagraphic case, e.g. in Thiébaut & Conan (1995). The calculation of both gradients $\frac{\partial J^{\text{foc}}}{\partial \boldsymbol{\phi}_u[k]}$ and $\frac{\partial J^{\text{foc}}}{\partial \boldsymbol{\phi}_d[l]}$ gives

$$\begin{aligned} \frac{\partial J^{\text{foc}}}{\partial \boldsymbol{\phi}_u[k]} &= 2\Im\left\{ \boldsymbol{\psi}^*[k] \left[\text{FT}\left(\frac{\partial J^{\text{foc}}}{\partial\, \boldsymbol{h}_c^{\text{foc}}} (\boldsymbol{\Psi} - \eta_0 \boldsymbol{\Psi_d}) \right) \right] \right\}[k] \\ &- 2\Re\left(\frac{\partial \eta_0}{\partial \boldsymbol{\phi}_u[k]} \sum_t \frac{\partial J^{\text{f}}}{\partial\, \boldsymbol{h}_c^{\text{foc}}} \boldsymbol{\Psi}^* \boldsymbol{\Psi_d} \right) \\ &+ \frac{\partial |\eta_0|^2}{\partial \boldsymbol{\phi}_u[k]} \sum_t \frac{\partial J^{\text{f}}}{\partial\, \boldsymbol{h}_c^{\text{foc}}} |\boldsymbol{\Psi_d}|^2 \end{aligned} \tag{A.4}$$

$$\begin{aligned} \frac{\partial J^{\text{foc}}}{\partial \boldsymbol{\phi}_d[l]} &= 2\Im\Bigg((\boldsymbol{\psi}^*[l] - \eta_0^* {\boldsymbol{\psi_d}}^*[l]) \\ &\times \left\{ \text{FT}\left[\frac{\partial J^{\text{f}}}{\partial\, \boldsymbol{h}_c^{\text{foc}}} (\boldsymbol{\Psi} - \eta_0 \boldsymbol{\Psi_d}) \right] \right\}[l] \Bigg). \end{aligned} \tag{A.5}$$

With $\Im$ and $\Re$ the imaginary and real part (respectively), and

$$\begin{aligned} \frac{\partial \eta_0}{\partial \boldsymbol{\phi}_u} &= j \boldsymbol{P}_u^2 e^{j\boldsymbol{\phi}_u} \\ \boldsymbol{\psi}(\boldsymbol{\phi}_u, \boldsymbol{\phi}_d) &= \boldsymbol{P}_d e^{j(\boldsymbol{\phi}_u + \boldsymbol{\phi}_d)} \qquad \boldsymbol{\Psi}(\boldsymbol{\phi}_u, \boldsymbol{\phi}_d) = \text{FT}^{-1}(\boldsymbol{\psi}) \\ \boldsymbol{\psi_d}(\boldsymbol{\phi}_d) &= \boldsymbol{P}_d e^{j\boldsymbol{\phi}_d} \qquad \boldsymbol{\Psi}_d(\boldsymbol{\phi}_d) = \text{FT}^{-1}(\boldsymbol{\psi_d}). \end{aligned} \tag{A.6}$$

Since the phases are expanded on a Zernike basis, we need the gradients of J^{foc} with respect to the Zernike coefficients a_{x_i} of phase $\boldsymbol{\phi}_x$. These gradients are given by the expression (Mugnier et al. (2001)):

$$\frac{\partial J^{\text{foc}}}{\partial a_{x_i}} = \sum_k \frac{\partial J^{\text{foc}}}{\partial \boldsymbol{\phi}_x[k]} Z_i[k]. \tag{A.7}$$

Flux α and constant background β are also analytically estimated during the minimization, considering that

$$J^{\text{p}}[t] = \frac{1}{2}\sum_t \left| \frac{-\boldsymbol{i}_c^{\text{p}}[t] + \alpha.\boldsymbol{h}_{\text{det}}[t] \star \boldsymbol{h}_c^{\text{p}}[t] + \beta}{\boldsymbol{\sigma}_n^{\text{p}}[t]} \right|^2 \tag{A.8}$$

Where p is for "foc" (focused) or "div" (diverse). For the sake of simplicity, we shall omit the variable t. We have

$$\begin{aligned} \frac{\partial J^{\text{p}}}{\partial \alpha} &= \alpha \sum \frac{(\boldsymbol{h}_{\text{det}} \star \boldsymbol{h}_c^{\text{p}})^2}{{\boldsymbol{\sigma}_n^{\text{p}}}^2} + \beta \sum \frac{\boldsymbol{h}_{\text{det}} \star \boldsymbol{h}_c^{\text{p}}}{{\boldsymbol{\sigma}_n^{\text{p}}}^2} \\ &- \sum \frac{(\boldsymbol{h}_{\text{det}} \star \boldsymbol{h}_c^{\text{p}}) \boldsymbol{i}_c^{\text{p}}}{{\boldsymbol{\sigma}_n^{\text{p}}}^2} \\ \frac{\partial J^{\text{p}}}{\partial \beta} &= \alpha \sum \frac{\boldsymbol{h}_{\text{det}} \star \boldsymbol{h}_c^{\text{p}}}{{\boldsymbol{\sigma}_n^{\text{p}}}^2} + \beta \sum \frac{1}{{\boldsymbol{\sigma}_n^{\text{p}}}^2} - \sum \frac{\boldsymbol{i}_c^{\text{p}}}{{\boldsymbol{\sigma}_n^{\text{p}}}^2} \end{aligned} \tag{A.9}$$

Which gives us, in a matricial form:

$$\begin{pmatrix} \sum \frac{(\boldsymbol{h}_{\text{det}} \star \boldsymbol{h}_c^{\text{p}})^2}{{\boldsymbol{\sigma}_n^{\text{p}}}^2} & \sum \frac{\boldsymbol{h}_{\text{det}} \star \boldsymbol{h}_c^{\text{p}}}{{\boldsymbol{\sigma}_n^{\text{p}}}^2} \\ \sum \frac{\boldsymbol{h}_{\text{det}} \star \boldsymbol{h}_c^{\text{p}}}{{\boldsymbol{\sigma}_n^{\text{p}}}^2} & \sum \frac{1}{{\boldsymbol{\sigma}_n^{\text{p}}}^2} \end{pmatrix} \begin{pmatrix} \alpha \\ \beta \end{pmatrix} = \begin{pmatrix} \sum \frac{(\boldsymbol{h}_{\text{det}} \star \boldsymbol{h}_c^{\text{p}}) \boldsymbol{i}_c^{\text{p}}}{{\boldsymbol{\sigma}_n^{\text{p}}}^2} \\ \sum \frac{\boldsymbol{i}_c^{\text{p}}}{{\boldsymbol{\sigma}_n^{\text{p}}}^2} \end{pmatrix}. \tag{A.10}$$

A simple matrix inversion gives us the analytical estimation of the flux α and the background β for each iteration.

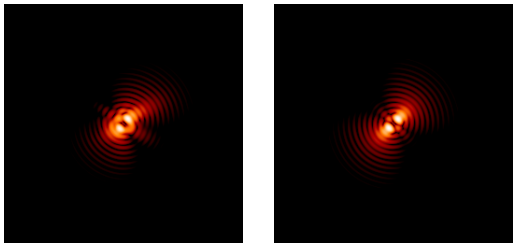

Fig. B.1. Coronagraphic diversity images computed for an aberration $\phi_u + \phi_{div}$ upstream, ϕ_d downstream of (left) and the only diversity aberration ϕ_{div} (right). The shape of both images is mainly driven by diversity aberration.

Appendix B: Tip-tilt estimation downstream of the coronagraph

The tip-tilt downstream of the coronagraph (which represents the image position on the detector) strongly limits COFFEE's performance. Indeed, we determine that the phase estimation was accurate when -100 nm RMS $\leq a_i \leq 100$ nm RMS, with a_i the Zernike coefficient for tip or tilt ($i \in \{2, 3\}$). Beyond this range, COFFEE is unable to properly estimate both phases ϕ_u and ϕ_d. Such a phenomenon strongly limits COFFEE's performance on a bench, since its utilization requires a restrictive location of the PSF on the detector.

To get rid of this limitation, we have developed a simple and fast method of estimating the tip-tilt downstream of the coronagraph before COFFEE's estimation, based on the diversity image. This image is created by adding a known aberration $\phi_{div} = a_4^{div} Z_4 + a_5^{div} Z_5$ ($a_4^{div} = a_5^{div} = 80$ nm RMS) to ϕ_u. Since the amplitude of this aberration is important ($\sigma_{\phi_{div}} = 113$ nm RMS), the speckles we have in the coronagraphic diversity image mainly originate in this diversity aberration. This is illustrated in Figure B.1, where we show two diversity images: one computed with randomly generated phases ϕ_u (WFE 30 nm RMS), ϕ_d (WFE 10 nm RMS), and another computed with no aberrations other than the diversity ones.

As one can see in Figure B.1, we can clearly identify the aberrations which originate in the diversity ϕ_{div}. The principle of our method lies in the research of these well-known aberrations (since we know the phase ϕ_{div} we introduce) in the diversity image i_c^{d} by comparing it with a theoretical diversity image $i_{c_{th}}^{\mathrm{d}}$, calculated with no other aberrations than the diversity ones:

$$\boldsymbol{i}_{c_{th}}^{\mathrm{d}} = \boldsymbol{h}_{\mathrm{det}} \star \boldsymbol{h}_c(\boldsymbol{\phi}_{div}, \boldsymbol{\phi}_d = 0). \tag{B.1}$$

The comparison of $i_{c_{th}}^{\mathrm{d}}$ with i_c^{d} is performed using the method developed by Gratadour et al. (2005), which consists in minimizing the following criterion J_{TT}

$$J_{\mathrm{TT}}(x, y) = \left\| \frac{\boldsymbol{i}_c^{\mathrm{div}}(x_o, y_o) - \boldsymbol{i}_{c_{th}}^{\mathrm{div}}(x_o, y_o) \star \boldsymbol{\delta}(x_o - x, y_o - y)}{\boldsymbol{\sigma}_n^{\mathrm{div}}} \right\|^2, \tag{B.2}$$

Where $\boldsymbol{\delta}$ is the dirac function. Minimization of J_{TT} gives us the shift $[x_M, y_M]$between both images. It is then possible to calculate the corresponding tip (a_2) and tilt (a_3) downstream of the coronagraph knowing the image sampling s:

$$a_2 = \frac{\pi}{2s} x_M \qquad a_3 = \frac{\pi}{2s} y_M. \tag{B.3}$$

Finally, these estimated tip-tilt values are given to COFFEE as an input of the minimization, and are used as initial values to begin phase reconstruction. This method performs, on our experimental images, a fast preliminary estimation ($\sim$ 1 second for a 256×256 image) of the tip-tilt downstream of the coronagraph with an accuracy of 1.5 nm RMS, which is far enough, compared to the level of accuracy (± 100 nm RMS) required by COFFEE.

References

Baudoz, P., Boccaletti, A., Baudrand, J., & Rouan, D. 2006, in Proc. IAU Colloquium

Baudoz, P., Mazoyer, J., Mas, M., Galicher, R., & Rousset, G. 2012, in Ground-based and Airborn Intrusmentation for Astronomy IV, Vol. 8446, Proc. Soc. Photo-Opt. Instrum. Eng.

Beuzit, J.-L., Feldt, M., Dohlen, K., et al. 2007, in Proceedings of the conference In the Spirit of Bernard Lyot: The Direct Detection of Planets and Circumstellar Disks in the 21st Century., ed. P. Kalas, University of California, Berkeley, CA, USA

Bordé, P. J. & Traub, W. A. 2006, Astrophys. J., 638

Born, M. & Wolf, E. 1989, Principles of Optics (Pergamon Press)

Give'on, A., Belikov, R., Shaklan, S., & Kasdin, J. 2007, Opt. Express, 15

Gonsalvez, R. 1982, Opt. Eng., 21

Gratadour, D., Mugnier, L. M., & Rouan, D. 2005, Astron. Astrophys., 443, 357

Guyon, O., Matsuo, T., & Angel, R. 2009, Astrophys. J., 693

Guyon, O., Roddier, C., Graves, J., et al. 1999, Pub. Astron. Soc. Pacific, 111

Kalas, P., Graham, J. R., Chiang, E., et al. 2008, Science, 332

Lagrange, A.-M., Gratadour, D., Chauvin, G., et al. 2009, Astron. Astrophys., 493, L21

Macintosh, B. A., Graham, J. R., Palmer, D. W., et al. 2008, in Adaptive Optics Systems, Vol. 7015, Proc. Soc. Photo-Opt. Instrum. Eng.

Marois, C., Macintosh, B., Barman, T., et al. 2008, Science, 322

Mugnier, L. M., Blanc, A., & Idier, J. 2006, in Advances in Imaging and Electron Physics, ed. P. Hawkes, Vol. 141 (Elsevier), 1–76

Mugnier, L. M., Fusco, T., & Conan, J.-M. 2004, J. Opt. Soc. Am. A, 21, 1841

Mugnier, L. M., Robert, C., Conan, J.-M., Michau, V., & Salem, S. 2001, J. Opt. Soc. Am. A, 18, 862

Noll, R. J. 1976, J. Opt. Soc. Am., 66, 207

Press, W. H., Teukolsky, S. A., Vetterling, W. T., & Flannery, B. P. 2007, Numerical Recipes : the art of scientific computing (Cambridge University Press)

Roddier, F. & Roddier, C. 1997, Pub. Astron. Soc. Pacific, 109

Sauvage, J.-F., Fusco, T., Rousset, G., & Petit, C. 2007, J. Opt. Soc. Am. A, 24, 2334

Sauvage, J.-F., Mugnier, L., Paul, B., & Villecroze, R. 2012, Opt. Lett., 37, 4808

Sauvage, J.-F., Mugnier, L. M., Rousset, G., & Fusco, T. 2010, J. Opt. Soc. Am. A, 27, A157

Soummer, R., C.Aime, & Falloon, P. 2003, Astron. Astrophys., 397

Soummer, R., L.Pueyo, A.Sivaramakrishnan, & Vanderbei, R. 2007, Opt. Express, 15

Thiébaut, E. 2002, in Astronomical Data Analysis II, Vol. 4847, Proc. Soc. Photo-Opt. Instrum. Eng., 174–183

Thiébaut, E. & Conan, J.-M. 1995, J. Opt. Soc. Am. A, 12, 485

Trauger, J., Give'on, A., Gordon, B., et al. 2010, in Tecniques and Instrumentation for Detection of Exoplanets III, Vol. 6693, Proc. Soc. Photo-Opt. Instrum. Eng.

Wallace, J. K., Burruss, R. S., Bartos, R. D., et al. 2010, in Adaptive Optics Systems II, Vol. 7736, Proc. Soc. Photo-Opt. Instrum. Eng.